Bitesize bundles F-actin and influences actin remodeling in syncytial *Drosophila* embryo development

Authors: Anna R. Yeh[1], Gregory J. Hoeprich[2], Anthony McDougal[1], Bruce L. Goode[2], Adam C. Martin[1]

[1]Department of Biology, Massachusetts Institute of Technology, Cambridge, MA, USA

[2]Department of Biology, Brandeis University, Waltham, MA, USA

Corresponding author: Adam C. Martin, acmartin@mit.edu

Abstract

Actin networks undergo rearrangements that influence cell and tissue shape. Actin network assembly and organization is regulated in space and time by a host of actin binding proteins. The *Drosophila* Synaptotagmin-like protein, Bitesize (Btsz), is known to organize actin at epithelial cell apical junctions in a manner that depends on its interaction with the actin-binding protein, Moesin. Using RNAi, we showed that Btsz functions at earlier, syncytial stages of *Drosophila* embryo development. Btsz is required to stabilize pseudo-cleavage furrows that prevent metaphase spindle collisions and nuclear fallout prior to cellularization. While previous studies have focused on Btsz function through Moesin, we find that phosphorylated Moesin localized to the nuclear envelope and was not enriched at pseudo-cleavage furrows, suggesting a Moesin-independent function for Btsz in syncytial embryos. Consistent with this, mutants that affected all Moesin binding domain isoforms did not recapitulate pan-isoform Btsz depletion and we find that the C-terminal half of Btsz cooperatively binds to and bundles

F-actin. We propose that Synaptotagmin-like proteins directly regulate actin organization during syncytial *Drosophila* development.

Introduction

During animal development, actin networks are tightly regulated and undergo dynamic rearrangements to promote cell and tissue morphogenesis (Camuglia et al., 2021; Lecuit and Yap, 2015; Sokac et al., 2023). However, the range of mechanisms that control actin network assembly and organization during development is still not fully understood. Actin networks must be regulated at four major levels. First, is the control of assembly. The nucleation and assembly of monomeric G-actin (globular actin) into polymeric F-actin (filamentous actin) are tightly regulated in both time and space. Spontaneous nucleation of actin is inhibited by many factors *in vivo* (Plastino and Blanchoin, 2019). Therefore, actin nucleators and polymerizers such as the formin, Diaphanous (Dia), as well as the Arp2/3 complex are essential in driving actin network formation. Dia assembles actin structures composed of linear (unbranched) filaments, whereas Arp2/3 complex assembles branched actin filament networks. Next, is the spatial organization of filaments into higher-order structures, or networks, which involves a plethora of actin binding and bundling/crosslinking proteins such as Fascin/Singed, Filamin/Cheerio and Fimbrin (Cant et al., 1994; Davidson et al., 2019; Krueger et al., 2019; Tilney et al., 2000). These networks are important for structure, transport, and transducing mechanical forces across the organism. Crosslinking actin filaments not only governs the network's architecture but also its rigidity and contractile properties (Koenderink and Paluch, 2018). Third is the regulated disassembly or turnover of actin networks, which is orchestrated by a team of actin binding proteins that includes cofilin, AIP1, coronin, twinfilin, and cyclase-associated protein (CAP) (Goode et al., 2023). Finally, the cortical actin network must be connected to the cell plasma

membrane through actin-binding proteins in order to provide structure and help induce cell shape changes (Chugh and Paluch, 2018). The ERM (Ezrin Radixin Moesin) family of proteins plays an essential role in this process (Algrain et al., 1993; Gould et al., 1989). When activated by phosphorylation through kinases, ERM proteins undergo a conformational change, exposing an F-actin binding and membrane protein-binding site through which it tethers F-actin to membranes (Gary and Bretscher, 1995; Zaman et al., 2021). Therefore, each cell must coordinate actin nucleation, assembly, and disassembly with higher-order actin network organization and membrane-to-cortex attachment.

The early *Drosophila* embryo provides an optimal system in which to study actin regulation due to its dynamic actin network rearrangements. At the earliest stages of development, the embryo is a syncytium consisting of one cell with multiple nuclei in a shared cytoplasm. The syncytium undergoes multiple rounds of synchronous modified cell divisions lacking cytokinesis and intervening gap phases, called nuclear divisions (Figure 1A) (Foe et al., 2000). Nuclear cycles (NC) 1-9 occur in the yolk at the center of the embryo, and nuclei migrate to the apical surface of the embryo for NC 10-13 (Foe et al., 2000). Centrosomes then help direct the formation of F-actin structures called ‘caps’ (Stevenson et al., 2002, 2001), which are positioned above the syncytial nuclei. During each nuclear cycle, F-actin assembly drives the growth of actin caps that expand into one another (Figure 1A). Collisions between neighboring caps lead to the formation of pseudo-cleavage furrows, structures made up of both actin and membrane that serve to compartmentalize mitotic spindles (Zhang et al., 2018) (Figure 1A). Pseudo-cleavage furrows act as a barrier between dividing spindles and are essential for proper nuclear

divisions. Perturbing pseudo-cleavage furrows with drugs or depleting actin regulatory proteins often results in spindle collisions (Afshar et al., 2000; Callaini et al., 1992; Spracklen et al., 2019; Sullivan et al., 1993; Webb et al., 2009; Zallen et al., 2002).

In addition to actin assembly, membrane trafficking is essential for syncytial blastoderm development. When membrane trafficking is perturbed by knocking down components of the trafficking machinery, such as Nuf and Rab11, pseudo-cleavage furrows are shorter and resemble those in embryos defective in actin assembly (Cao et al., 2008; Holly et al., 2015; Riggs et al., 2003; Rikhy et al., 2015; Rothwell et al., 1998; Sherlekar et al., 2020). Together, these findings indicate that actin network reorganization is coupled with membrane remodeling to create pseudo-cleavage furrows. However, there is still much to uncover about the roles of actin and/or membrane remodelers play in this process.

Synaptotagmin-like proteins (Slps) are potential candidates for coupling actin and membrane remodeling during syncytial blastoderm development. Slps are conserved across vertebrates and many invertebrates. Vertebrate Slps are characterized by an N-terminal Slp homology domain (SHD) and two C-terminal C2 domains (Figure 1B). The mammalian SHD interacts with the GTPase Rab27, and the C2 domain consists of the C2A and C2B domains that bind membrane, sometimes in a calcium-dependent manner (Fukuda, 2002; Gálvez-Santisteban et al., 2012). Specifically, the C2A domain binds with high affinity to PI(4,5)P_2 or PI(3,4,5)P_3 and the C2B domain binds with high affinity to PI(4,5)P_2 (Gálvez-Santisteban et al., 2012; Lyakhova and Knight, 2014). A family of proteins related to Slps are Slac2s, Synaptotagmin-like proteins lacking C2 domains, which contain the SHD at their N-terminus but contain a unique C-terminus

95 lacking the C2 domains (Figure 1B). Slac2 proteins function as adaptor proteins for
96 cargo transport, interacting with Rab27A via their SHD, as well as Myosin Va via their
97 myosin-binding sites found in the middle of Slac2 (Fukuda et al., 2002). Interestingly,
98 the C-termini of Slac2-a and Slac2-c also bind G- and F-actin (Fukuda et al.,
99 2002). Both Slps and Slac2s are Rab27 effectors important for vesicle secretion. For
100 example, Slp4 is necessary for proper exocytosis and granule docking in the pancreas
101 (Mizuno et al., 2016). During *de novo* epithelial formation, Slp2-a is required for
102 targeting vesicles to the apical surface in a PIP_2 dependent manner, and Slp4-a couples
103 these vesicles to apical plasma membrane to generate lumen (Gálvez-Santisteban et
104 al., 2012). Overall, there are six Slp genes and three Slac2 genes in mammals.
105 *Drosophila* encodes a single Slp gene, *Bitesize* (*Btsz*) that plays a role in actin
106 cytoskeleton organization (Pilot et al., 2006b) similar to mammalian Slp4/granuphilin.
107 Pilot et al. showed that Btsz is essential for maintaining adherens junctions and
108 epithelial integrity. They discovered that Btsz binds phosphoinositides and that certain
109 Btsz isoforms interact with the membrane-cortex crosslinker, Moesin (Moe), via a
110 Moesin binding domain (MBD) (Figure 1C, D). During tracheal morphogenesis, Btsz
111 recruits Moesin to the luminal membrane to promote proper actin organization
112 (JayaNandanan et al., 2014). Therefore, previous work has established the importance
113 of Btsz in regulating the actin cytoskeleton through Moesin. However, alternative
114 splicing generates nine different Btsz isoforms and most of them lack the exon that
115 encodes the MBD (Figure 1C). This raises the question of whether Btsz has additional,
116 distinct functional roles in development.

117 In this study, we discovered a role for Btsz in regulating pseudo-cleavage furrow
118 morphology and stability during syncytial stages of *Drosophila* embryo development,
119 which in turn impacts spindle and nuclear morphology. This function of Btsz is
120 mediated, at least in part, through functions beyond Moesin recruitment. We
121 demonstrated this by examining phospho-Moesin localization, comparing genetic alleles
122 that affect distinct sets of Btsz isoforms, and examining isoform-specific expression in
123 the early embryo. We found that the C terminus of Btsz binds to F-actin and bundles F-
124 actin *in vitro*, suggesting a direct role for Btsz in regulating actin architecture.
125

126 **Results**

127 **Btsz is required for actin remodeling during syncytial blastoderm development**

128 To examine Btsz function in early development, we used an RNAi line to maternally
129 deplete embryos of Btsz (Figure S1A). This shRNA targets a sequence in the 3' UTR
130 shared by all isoforms, while primers used for RT-PCR detected MBD and Exon 4
131 containing isoforms (Figure S1A and B). Past work on Btsz focused on isoforms
132 containing the Moesin-binding domain (MBD, Exon 8) and their roles during gastrulation
133 in regulating actin organization, epithelial integrity, and lumen formation (JayaNandanan
134 et al., 2014; Pilot et al., 2006b). Upregulation of Btsz isoforms containing the MBD at the
135 mid-blastula transition was noted in previous studies (Pilot et al., 2006a). Knock-down of
136 all Btsz isoforms revealed striking defects in syncytial embryo development as well as
137 defects after epithelium formation, during gastrulation. We found that 60% of Btsz-RNAi
138 embryos displayed syncytial or cellularization defects compared to 13% of control
139 embryos and 92% of Arp3 RNAi embryos, which we used as a positive control (Figure

140 S1C). Because defects prior to gastrulation in Btsz-depleted embryos have not been
141 described, and the syncytial blastoderm is an excellent system in which to study actin
142 remodeling, we further investigated Btsz function in the syncytial blastoderm.

143 To determine Btsz function in syncytial stages of embryonic development, we
144 visualized actin in live embryos by driving mCherry::MoesinABD (mCh::Moe) expression
145 with the maternal Gal4 driver to observe actin cap and pseudo-cleavage furrow
146 structure and dynamics (Xie et al., 2021). We found that Btsz depletion affected the
147 organization of F-actin compartments above the nuclei (Figure 2A; Video 1). We
148 measured nuclear F-actin compartment size once the caps had finished expanding in
149 control and Btsz-RNAi embryos. We quantified cycle 12 compartments because of good
150 nuclear spacing and it has a high number of caps without the caps being too crowded.
151 Our results show that in Btsz-depleted embryos, the average compartment area is
152 smaller compared to those of control embryos (Figure 2A-B). When comparing the
153 distribution of compartment areas, there is a bimodal distribution of compartment sizes
154 and a greater proportion of small compartments (<80 μm^2) in Btsz-RNAi embryos
155 compared to the control (Figure 2B-B'').

156 Actin cap expansion and subsequent collisions between neighboring caps drive
157 pseudo-cleavage furrow formation and growth (Zhang et al., 2018) so we hypothesized
158 that pseudo-cleavage furrows would be affected in Btsz-RNAi embryos. Interestingly,
159 small actin caps in Btsz-depleted embryos still formed pseudo-cleavage furrows
160 between nuclei. Live imaging of actin in pseudo-cleavage furrows did reveal that a
161 higher frequency of furrows prematurely retract during mitosis in Btsz-RNAi embryos
162 (Figure 2C, D; Video 2). These unstable furrows formed normally (Figure 2C, yellow

163 arrows) but receded during metaphase, resulting in furrows that are either very short or
164 no longer visible (Figure 2C, red arrows). Because furrow regression could reflect a
165 membrane trafficking defect (Holly et al., 2015; Riggs et al., 2003; Rikhy et al., 2015;
166 Rothwell et al., 1998), we tested whether Btsz-RNAi affected ER or golgi structure.
167 Btsz-RNAi did not affect ER or golgi morphology (Figure S2A). Pseudo-cleavage
168 furrows that formed properly and did not retract in Btsz-RNAi embryos reached their
169 maximum length and were comparable in length to wild-type furrows (Figure S2B, C).
170 However, the straightness of the furrows projecting into the cytoplasm were often
171 abnormal in Btsz-RNAi embryos – furrows were more bent than in wild type, which
172 could be observed across the embryo by comparing the outlines of pseudo-cleavage
173 furrows at different depths (Figure S2D). Although F-actin levels were equivalent
174 between control and Btsz-RNAi pseudo-cleavage furrow, the different morphology and
175 stability and the absence of a change in ER/golgi morphology suggested that the
176 mechanics or structure of these furrows is compromised.
177

178 **Btsz depletion leads to spindle collision and nuclear defects**

179 Because pseudo-cleavage furrows are essential for preventing spindle collisions during
180 each nuclear cycle, we assessed the integrity of the nuclear divisions in Btsz-depleted
181 embryos. Using the microtubule plus-end-tracking protein CLIP170 fused with GFP to
182 visualize spindles, we found that aberrant spindle morphology accompanied *Btsz* knock-
183 down (Figure 3A, C). In Btsz-depleted embryos, spindles were often abnormally fused
184 between neighboring nuclei (Figure 3A). This spindle collision phenotype has been
185 noted in various conditions where proteins that regulate actin are disrupted (Dia, Arp2/3,

186 Par1, APC2, Abl, Nuf, Rab11, etc.) (Grevengoed et al., 2003; Jiang and Harris, 2019;
187 McCartney et al., 2001; Riggs et al., 2003; Rothwell et al., 1998; Webb et al., 2009;
188 Zhang et al., 2018).

189 Proper actin cytoskeleton regulation is important for centrosome migration to
190 opposite poles during nuclear division cycles (Cao et al., 2008). Centrosome separation
191 was abnormal in Btsz-depleted embryos (Figure 3B) with centrosomes failing to migrate
192 to 180° opposite each other prior to nuclear envelope breakdown more often than in
193 wild-type embryos (Figure 3B, C'). Both the distance between centrosomes (Figure 3C'')
194 and spindle length (Figure 3C''') were shorter in Btsz-depleted embryos compared to
195 wild-type embryos. These phenotypes were reminiscent of those observed in other actin
196 and APC2 mutants (Cao et al., 2008; McCartney et al., 2001). Fixed imaging of both F-
197 actin and nuclei during cellularization revealed heterogeneity in compartment sizes and
198 nuclear morphology in Btsz-RNAi embryos, indicative of improper nuclear divisions that
199 occurred earlier in the syncytium (Figure 3D).

200 Visualizing both F-actin and spindles confirmed that furrow breakages in the
201 Btsz-RNAi background led to two sets of spindles in the same compartment (Figure
202 S2E). These spindle abnormalities preceded massive nuclear fallout from the cell cortex
203 during syncytial stages and preceding cellularization, observed through live imaging the
204 nuclear marker Histone::GFP (Figure 3E, yellow arrows; Video 3). Quantification of
205 relative nuclear density showed that there are fewer nuclei in Btsz-depleted embryos
206 compared to the control (Figure 3F), likely a consequence of the pseudo-cleavage
207 furrow defects (Figure 2C) and subsequent nuclear fallout. Overall, these results

208 demonstrate a critical role for Btsz in embryo development, prior to its known role in
209 epithelial integrity during gastrulation.
210
211 **Btsz has function(s) in the syncytium that do not depend on localizing Moesin**
212 Prior work showed that Btsz functions with Moesin during gastrulation (Pilot et
213 al., 2006b) and Moesin has been suggested to function in syncytial nuclear divisions
214 (Vilmos et al., 2016). To determine how Btsz regulates syncytial divisions we examined
215 Moesin and Btsz localization in the syncytial embryo. We first examined the localization
216 of phospho-Moesin (pMoesin), the activated form of Moesin, using a previously
217 published antibody (Carreno et al., 2008). pMoesin staining was not enriched in actin
218 caps or pseudo-cleavage furrows (Figure 4A, Figure S2F). However the pMoesin
219 antibody clearly labeled a perinuclear structure as has been described previously
220 (Vilmos et al., 2009). We found this pMoesin-containing structure colocalized with Lamin
221 B and was present at different cell cycle stages, in a manner that resembles Lamin B
222 staining (Figure 4A). Because a nuclear excluded mutant of Moesin (fused to nuclear
223 export sequence) also exhibits this staining pattern, we suggest that pMoesin, in part, is
224 coating the nuclear envelope (Bajusz et al., 2021). BtszF is one of the shortest Btsz
225 isoforms (Figure 1C), containing only the C2 domains that are necessary for proper
226 localization and one additional exon. Because past work indicated that the C2 domains
227 are responsible for Btsz localization (Pilot et al., 2006b), we visualized this tagged
228 isoform to infer Btsz localization. Unlike pMoesin, BtszF localized to pseudo-cleavage
229 furrows and plasma membrane infoldings from the actin caps (Tam and Harris, 2024)

230 (Figure 4B). Thus, Btsz and pMoesin localize to different subcellular structures in
231 syncytial embryos.

232 We next determined which Btsz isoforms were expressed in the early embryo.
233 Consistent with what was previously reported, we found that Moesin Binding Domain
234 (MBD, Exon8) isoforms and Exon 4-6-containing exons were present in the early
235 embryo, consistent with prior work (Pilot et al., 2006b) (Figure S1A and B). Because
236 BtszI has the MBD exon and most other exons, we distinguished between BtszI and
237 non-MBD isoforms by using isoform specific primers (Figure 1C, green arrows). We
238 found that non-MBD isoforms, as well as BtszI, increased in expression at the MZT ~ 2-
239 4 hr time point (Figure 4C). Detection of BtszI and non-MBD isoforms was inconsistent
240 at 0-2 hours, suggesting that there is low or no expression of these isoforms at this
241 stage. Overall, this data shows that MBD, non-MBD, and BtszI isoforms are expressed
242 in the early embryo.

243 We next tested whether pMoesin localization is compromised in Btsz-RNAi
244 embryos with syncytial defects. We found that Btsz-RNAi did not affect pMoesin
245 intensity or localization, suggesting that the syncytial defects in Btsz-RNAi did not result
246 from activated Moesin recruitment defects (Figure 4D). Taken together, the distinct
247 localizations of Btsz and Moesin, the absence of Moesin at pseudo-cleavage furrows,
248 failure of Btsz-RNAi to affect Moesin localization, and the presence of both MBD and
249 non-MBD isoforms suggests that Bitesize has some functions that are Moesin
250 independent.

251

252 **Btsz mutants suggest Moesin-independent function(s) during syncytial cell**
253 **divisions**

254 While we found that Bitesize expression was upregulated at cellularization
255 (Figure 4C), Btsz-RNAi did not significantly affect cellularization furrow canal F-actin
256 levels (Figure S3A and S3B). Cellularization was sometimes uneven in Btsz-RNAi
257 embryos most often exhibiting a delay at the posterior pole (Figure S3C). Because
258 perturbations that disrupt nuclear density result in significant asynchrony in cell cycle
259 times (Deneke et al., 2019), it is likely that Btsz-RNAi cellularization phenotypes reflect
260 earlier spindle collisions. However, abnormal nuclear density at cellularization (Figure
261 5C) gave us a robust metric to compare the severity of the nuclear fallout resulting from
262 spindle collisions during syncytial divisions (Video 3).

263 Because Btsz-RNAi embryos exhibited an obvious nuclear density phenotype
264 and because live actin markers occasionally modified the furrow canal phenotypes
265 (Spracklen et al., 2014), we visualized nuclear compartments using the non-muscle
266 myosin II marker, Spaghetti squash::GFP (Sqh::GFP) (Figure 5C,D). Btsz-RNAi resulted
267 in massive nuclear fallout, which was reflected in abnormal nuclear density by the time
268 of cellularization, with the myosin network coating the membrane spanning the space
269 between nuclei. Note that there were some more mildly affected embryos in the Btsz-
270 RNAi data, which likely reflected incomplete knock-down.

271 To determine Btsz function in syncytial stages, we examined mutants that affect
272 different sets of Btsz isoforms. The *btsz*$^{K13\text{-}4}$ mutant has a deletion in the MBD-
273 containing exon 8, which affects BtszC and BtszD, as well as the longest isoform, BtszI
274 (Serano and Rubin, 2003). Germline *btsz*$^{K13\text{-}4}$ mutant clones showed abnormal nuclear

density (Figure 5D) and actin caps that appeared to have lost nuclei at syncytial stages (Figure S4), but did not affect pMoesin localization (Figure 5E). The *btsz*$^{K13\text{-}4}$ mutant affecting all MBD isoforms, including BtszI, but not recapitulating the pan-isoform RNAi knock-down, again argues for Moe-independent functions during syncytial development. If this were the case, we would expect other isoforms to also contribute to syncytial development.

Therefore, we used CRISPR/Cas9 to engineer a *btsz* mutant (*btsz exon 4*) with an early truncation present in the majority of non-MBD isoforms and BtszI (Figure 5A-B). The *btsz exon 4* mutant affected nuclear density and also did not fully recapitulate the pan-isoform knock-down (Figure 5C and 5D). Surprisingly, we found that the *btsz exon 4* mutant affects the nuclear localization of pMoesin. In summary, the full activity of Btsz requires both sets of MBD and non-MBD isoforms and the phenotype does not depend on an effect on pMoesin localization, suggesting that there are Moesin-independent functions for Btsz in the syncytium.

Btsz C-terminus binds and bundles F-actin

Given the defects in actin-related processes exhibited by Btsz-RNAi and Btsz mutants, we hypothesized that Btsz, including non-MBD isoforms, may directly interact with F-actin. We examined Btsz function *in vitro* using the BtszB-C terminal fragment, which starts within exon 6 and contains the C2A and C2B domains shared by the majority of Btsz isoforms (Figure 6A). The BtszB C-terminal fragment does not contain the MBD. The purified C-terminal fragment of BtszB (BtszB-CT) demonstrated good expression and solubility.

298 We performed high-speed pelleting assays to test whether BtszB-CT binds to
299 actin filaments and low-speed pelleting assays to test whether BtszB-CT bundles F-
300 actin. In high-speed pelleting assays, a fixed concentration of BtszB-CT was mixed with
301 variable concentrations of F-actin, and then the amount of BtszB-CT bound to F-actin
302 was determined by analyzing the supernatant and pellet fractions on gels. With
303 increasing concentrations of F-actin, BtszB-CT shifted from the supernatant to the pellet
304 (Figure 6B). The data best fit a cooperative binding model with a binding affinity (K_d) of
305 0.45 μM and a Hill coefficient (h) of 2.9 (Figure 6C). In low-speed pelleting assays, F-
306 actin alone did not pellet significantly, but the addition of BtszB-CT shifted F-actin to the
307 pellet (Figure 6D and E), suggesting that BtszB-CT organizes F-actin into higher order
308 structures. These effects were confirmed independently through direct visualization in
309 TIRF microscopy assays, where BtszB-CT organized F-actin into bundles with
310 increased fluorescence and thickness (Figure 6F and G). Overall, these results show
311 that BtszB-CT binds directly and cooperatively to F-actin (K_d = 0.45 μM) and organizes
312 actin filaments into bundles, suggesting that all Btsz isoforms may bind and bundle F-
313 actin.
314

315 **Discussion**

316 Actin network organization must be tightly regulated for proper syncytial
317 blastoderm development. Our data reveal a novel role for Synaptotagmin-like protein
318 Btsz in organizing actin in the syncytial *Drosophila* embryo. We found that Btsz
319 depletion resulted in defects reminiscent of the phenotypes caused by other mutants
320 and perturbations that affect actin organization, including defective actin caps and

321 pseudo-cleavage furrows (Afshar et al., 2000; Stevenson et al., 2002; Zallen et al.,
322 2002). Although prior work implicated Moesin downstream of Btsz function, our
323 evidence suggested that Btsz syncytial function was independent of Moesin: 1)
324 pMoesin localization was peri-nuclear and not enriched at actin caps or pseudo-
325 cleavage furrows, 2) Btsz-RNAi resulted in a dramatic pseudo-cleavage furrow and
326 spindle collision phenotype, including abnormal, bent furrow structures, but did not
327 affect pMoesin localization, 3) we showed that most isoforms are expressed in the
328 early *Drosophila* embryo, including those lacking the MBD, 4) the *btsz*$^{K13\text{-}4}$ mutant
329 germline clones, which affect all MBD-containing isoforms including BtszI, did not
330 recapitulate the pan-isoform Btsz-RNAi depletion and did not affect pMoe
331 localization, 5) the *btsz exon 4* mutant, which affected isoforms lacking the MBD and
332 BtszI, had a nuclear density phenotype, and 6) we showed that a Btsz C-terminal
333 fragment (lacking the MBD) cooperatively binds to F-actin and promotes F-actin
334 bundling. This supports a model in which Btsz binds the membrane through its C2
335 domains and directly promotes actin bundling along the membrane. In the related
336 Slac2 protein, Melanophilin, the actin binding domain (ABD) is also at the C-
337 terminus, however, the Btsz C-terminus is more similar to Slp proteins (Kuroda et al.,
338 2003). The identification of Btsz C-terminal actin binding and bundling activity shows
339 a unique activity that extends to proteins of the Slp family. Future studies are needed
340 to identify Btsz' actin binding domain and to separate the many activities of Btsz,
341 membrane binding, pMoesin recruitment, and actin binding/bundling.
342

343 **Btsz regulates actin organization at multiple stages of early *Drosophila***
344 **embryo development**

345 Our *in vitro* data indicate that the Btsz C-terminus binds and bundles F-actin,
346 shedding light on how Btsz may regulate actin *in vivo* in a complementary manner to
347 previously published role through Moesin (JayaNandanan et al., 2014; Pilot et al.,
348 2006b; Zhang et al., 2018). Our data suggests that many isoforms could bind and
349 bundle F-actin and moreover we did not see Moesin localization perturbed in all
350 conditions that caused defects. In the syncytium, Btsz could promote actin filament
351 bundles generated by the formin Diaphanous (Jiang and Harris, 2019). BtszF contains
352 the C2 domains and localizes to syncytial pseudo-cleavage furrows; because all Btsz
353 isoforms contain the C2 domains responsible for membrane localization, it is possible
354 that all isoforms localize to pseudo-cleavage furrows. Btsz bundling may stabilize actin
355 at the pseudo-cleavage furrows and prevent their recession, as furrows in Btsz-depleted
356 embryos often fail and disappear. We also observe that the psuedo-cleavage furrows of
357 Btsz-depleted embryos appear to become more undulatory over time compared to
358 controls, although higher resolution imaging is required to determine whether this is the
359 result of a more global perturbation in F-actin organization in these embryos (Figure 2C,
360 Figure S2C). The development of undulations may be indicative of a mechanical
361 instability (in addition to the temporal instability discussed above), which could arise due
362 to a lack of actin organization. During oogenesis, the *Drosophila* Fascin homolog,
363 Singed, is required for actin bundling when rapid actin polymerization takes place to
364 provide structural integrity for these bundles (Cant et al., 1994). Btsz may function in a
365 similar way, stabilizing F-actin bundles against disassembly during a time of rapid actin

366 remodeling during syncytial nuclear divisions. However, an important next step will be to
367 make mutants that separate Btsz actin binding and bundling activities and determine
368 their in vivo function.

369 Btsz isoforms are upregulated at the MZT. Zygotic gene activity is present as
370 early as cycle 10, where transcription is required for patterns of nuclear density
371 (Blankenship and Wieschaus, 2001). The expression of many actin remodeling proteins
372 are developmentally upregulated at the MZT, which is necessary for cellularization.
373 These include Bottleneck, Nullo, Slam, Dunk, and Serendipity-α (Sry-α), are
374 developmentally upregulated at the MZT (He et al., 2016; Krueger et al., 2019; Lecuit et
375 al., 2002; Postner and Wieschaus, 1994; Schejter and Wieschaus, 1993; Simpson and
376 Wieschaus, 1990; Sokac and Wieschaus, 2008; Wenzl et al., 2010; Zheng et al., 2013).
377 Unlike Btsz, these genes have a simple structure and lack complex splicing patterns.
378 Unlike *nullo* or *sry-α*, Btsz does not affect F-actin levels in furrow canals during
379 cellularization (Figure S3A, B) (Postner and Wieschaus, 1994; Simpson and
380 Wieschaus, 1990), suggesting that Btsz functions to prevent spindle collisions and
381 nuclear fallout during syncytial divisions.

382 Actin bundles are also a key component of adherens junctions (AJs), which are
383 critical for cell-cell adhesion. The dynamic coupling of the F-actin network to adherens
384 junctions is necessary for propagating forces across cells (Gorfinkiel and Arias, 2007;
385 Jodoin, 2015; Maître et al., 2012; Martin et al., 2010; Roh-Johnson et al., 2012). E-
386 cadherin (E-cad) is an important component of AJs, and its localization is stabilized by
387 F-actin. Non-junctional E-cadherin localizes to pseudo-cleavage furrows during
388 metaphase so it is possible that Btsz also interacts with E-cadherin in the syncytium

389 (Rikhy et al., 2015). When Btsz is disrupted, so is actin organization which in turn
390 destabilizes E-cadherin, leading to defects in tissue integrity (Pilot et al., 2006b). It is
391 possible that multiple Btsz isoforms with distinct activities could collaborate bind and
392 bundle F-actin to organize actin at these junctions. Overall, we speculate that Btsz is a
393 multifunctional cytoskeletal organizer, coupling membrane-cortex anchoring and F-actin
394 bundling activities.
395

396 **Possible functions for Btsz in membrane trafficking**

397 An important question that remains unanswered is whether Btsz plays a role in
398 *Drosophila* regulating membrane trafficking like mammalian Slps. Our work here
399 focused primarily on Btsz's role in actin organization, yet actin regulation and membrane
400 regulation may be interrelated. For instance, the Nuclear fallout (Nuf) protein is required
401 for actin and membrane remodeling during the syncytial divisions through its role in
402 regulating trafficking (Riggs et al., 2003). In *nuf* mutants, pseudo-cleavage furrows are
403 defective leading to spindle collisions and the 'nuclear fallout' phenotype (Rothwell et
404 al., 1998).

405 One surprising result in our work was that *btsz exon 4* mutant disrupted
406 pMoesin's peri-nuclear localization, while the pan-isoform Btsz-RNAi knockdown did
407 not. Considering the close coupling between actin and membrane remodeling, it is
408 possible that the nuclear fallout phenotype is, in part, due to defects in vesicle
409 trafficking. Moreover, BtszF is present in puncta (Figure 4B) which may indicate a
410 potential role in membrane trafficking and/or Btsz localization at plasma membrane
411 invaginations associated with exocytosis (Tam and Harris, 2024). Interestingly, the N-

terminus of several Btsz isoforms contains a putative zinc finger domain similar to those that interact with the Rab GTPases. The *btsz exon 4* mutant truncates protein products after this zinc finger domain, which could have an effect on vesicle trafficking, pMoesin's recruitment to the peri-nuclear structure, or Moesin phosphorylation. Future work is required to dissect the nature of pMoe nuclear localization and its regulation by Btsz. However, our work has shown a Moesin-independent function for some Btsz isoforms .

Materials and Methods

Fly stocks and genetics

Fly stocks and crosses used in this study are listed in Supplementary File 1. For crosses involving maternal gene depletion and overexpression, flies expressing maternal Gal4 drivers were crossed to UAS-driven constructs and maintained at 25°C. Nonbalancer F1 females were crossed to nonbalancer F1 males, and F2 embryos were used for imaging.

For the *btsz exon 4* mutant, a deletion was generated at the endogenous Btsz locus using CRISPR-Cas9 as previously described (Gratz et al., 2015). Two 15 base pair (bp) gRNAs targeting sites in Btsz exon 4, roughly 500 bps apart, were identified using flyrnai.org/crispr and cloned into the pCFD5 plasmid. This vector was constructed and packaged by VectorBuilder and the vector ID is VB200707-1018qzm, which can be used to retrieve further information about the vector on vectorbuilder.com. The plasmid was injected into nanos-Cas9-expressing embryos by BestGene Inc (Chino Hills, California). Surviving adults were crossed to Dr/TM3 flies and the deletion was screened for using PCR. Flies with successfully a generated deletion were sequenced

435 for further analysis. For crosses involving *btsz exon 4*, crosses were set up using two
436 *btsz exon 4* lines of independent CRISPR alleles.

437 For crosses involving *btsz*$^{K13-4}$, the FLP-DFS technique was used to generate
438 mutant germline clones (Chou and Perrimon, 1992). We used *btszK13-4* alone and
439 sqh::GFP; *btsz*$^{K13-4}$ mutant stocks. Briefly, hsFLP;; Dr/TM3, Sb females were crossed to
440 FRT82B ovoD1/TM3, Sb males. hsFLP/Y;; FRT 82B ovoD1/Dr males were crossed to
441 *btsz*$^{K13-4}$ FRT/TM3, Sb or sqh::GFP; *btsz*$^{K13-4}$ FRT/TM3, Sb females. Larvae from this
442 cross were heat shocked for 2 hrs at 37°C for 3-4 days. hsFLP; + or sqh::GFP*; btsz*$^{K13-4}$
443 FRT/*ovoD* FRT females were crossed to OregonR males to collect embryos resulting
444 from the *btsz*$^{K13-4}$ germline clones.

445 The pUASt-mCherry::BtszB fly line was constructed using the coding sequence
446 of BtszB (generous gift from Thomas Lecuit, Collège de France). The vector used to
447 overexpress mCherry::Btsz in our study was constructed and packaged by
448 VectorBuilder (Chicago, Illinois). The vector ID is VB211103-1199vfw. This vector was
449 injected into attP40 flies and surviving adults were crossed to Sp/CyO flies. Presence of
450 the vector was screened for by presence of red eye color and confirmed with
451 subsequent PCR and sequencing.

452 **Live and fixed imaging**

453 Crosses were maintained at 25°C unless otherwise stated. Embryos were collected
454 from apple-juice agar plates and embryos were staged using Halocarbon 27 oil.
455 Embryos were then dechorionated in 50% bleach (Chlorox) for 2 minutes and rinsed
456 twice with water.

457 For live imaging, embryos were mounted on a slide with embryo glue (Scotch
458 tape dissolved in heptane). No. 1.5 coverslips were placed on the slide on either side of
459 the mounted embryos and a No.1 coverslip was used to cover the embryos and create
460 a chamber. This chamber was filled using Halocarbon 27 oil.

461 For fixed imaging involving Phalloidin staining, embryos were fixed using 4%
462 paraformaldehyde (Electron Microscopy Sciences) in 0.1M phosphate buffer at pH 7.4
463 with 50% heptane (Alfa Aesar) and manually devitellinated. Embryos were washed in
464 0.01% Triton X-100 in PBS (PBS-T), incubated in primary antibodies followed by
465 secondary antibodies (Supplementary File 1), and mounted onto a glass slide using
466 AquaPolymount (Polysciences).

467 Live and fixed images were taken using a Zeiss LSM 710 point scanning
468 confocal microscope with a 40x/1.2 C-Apochromat water objective lens or 63x/1.4 Plan-
469 Apochromat oil objective lens, an argon-ion, 405 nm diode, 594 nm HeNe, 633 HeNe
470 laser, and Zen software. Pinhole settings ranged from 1 to 2.5 Airy units. For two-color
471 live imaging, band-pass filters were set at ~410-513 nm for Hoechst, ~490–565 nm for
472 GFP, and ~590–690 nm for mCherry (mCh). For three-color imaging, band-pass filters
473 were set at ~480–560 nm for Alexa Fluor 488, ~580–635 nm for Alexa Fluor 568, and
474 ~660–750 nm for Alexa Fluor 647.

475 **Image processing and analysis**

476 Figure images were processed in FIJI or Matlab R2019b. For actin cap area and
477 nuclear fallout quantifications, images were run through a segmentation analysis
478 (detailed below) in Matlab. For all figures, brightness and contrast were adjusted
479 linearly. For Figures 2, 3, and 6, images were processed in FIJI with a Gaussian blur of

0.5. For Figures 7 and 4B, images were processed in FIJI with a Gaussian blur of 0.5 and using Subtract Background with a rolling ball radius of 50.0 pixels.

Actin cap and cellularization furrow quantifications

Actin cap area and nuclear fallout

Embryos expressing mCherry::Moe were used to visualize actin caps. To stage-match embryos, we scored the size and number of actin caps. We measured actin cap area during NC12 past the expansion phase of cap growth to minimize gaps in the actin network. This was roughly 4 minutes before pseudo-cleavage furrows reach their maximum depth during NC12. A maximum intensity projection (MIP) at this time point was then used in a segmentation pipeline in MATLAB detailed below and manual corrections were made in FIJI. To count nuclei, MIPs of embryos expressing Sqh::GFP were segmented using the same Matlab procedure and FIJI was used to measure embryo area in the given field of view and to count nuclei.

1. The intensity of each pixel was scaled up by a factor of 1.25.
2. Ridge-like structures in the image were enhanced with FrangiFilter2D using the default parameters (Dirk-Jan Kroon (2022). Hessian based Frangi Vesselness filter (https://www.mathworks.com/matlabcentral/fileexchange/24409-hessian-based-frangi-vesselness-filter), MATLAB Central File Exchange); based on (Frangi et al., 1998).
3. The resulting image was blurred via a Gaussian blur of sigma 4-10 depending on the image using Matlab's imgaussfilt() function.

502 4. Seeds for a watershed segmentation were automatically determined using
503 the imregionalmin() function on the blurred, background-subtracted image.
504 5. The ridge-enhanced image from step 2 was blurred with a median filter of
505 size 11 pixels, then the seeds were imposed as local minima on this
506 image.
507 6. The watershed() function was used on this image to generate lines
508 corresponding to the boundaries between actin caps.

509 *Furrow actin intensity*

510 Cellularizing embryos were fixed and imaged to calculate the ratio of actin intensity in
511 the apical to basal regions in the furrows. FIJI was used to measure intensity. A ratio of
512 intensity was taken of the most apical and basal 2 μm of the furrows. Intensities were
513 normalized by rescaling values between 0 and 1 using $(I-I_{min})/(I_{max}-I_{min})$.

514 **Molecular biology**

515 For RNA extraction, thirty embryos were collected for each stage analyzed and ground
516 up in TRIzol reagent (Life Technologies, Inc.) using a motorized pestle mixer. mRNA
517 was extracted using TRIzol and chloroform. The aqueous phase was transferred into a
518 fresh tube and extraction continued using the Monarch RNA Cleanup Kit (NEB). The
519 extracted mRNA was treated with TURBO DNA-*free*™ (Invitrogen) and cDNA was
520 produced using Invitrogen SuperScript™ III First-Strand Synthesis System. Subsequent
521 PCR reactions were run with primers listed in (Supplementary File 1).

522 **Purification of BtszB**

523 Vectors of full-length BtszB and BtszB fragments were generated for protein expression
524 and purification (ABclonal Science Inc.). Full-length Btsz isoform B was insoluble in

525 bacteria and so we used the baculovirus system to express Btsz-B in Sf9 cells and
526 purified protein from those (ABclonal Science Inc).

527 **Purification and Labeling of Actin**

528 Rabbit skeletal muscle actin was purified from acetone powder (Spudich and Watt,
529 1971) generated from frozen ground hind leg muscle tissue of young rabbits (PelFreez).
530 Lyophilized acetone powder stored at -80°C was mechanically sheared in a coffee
531 grinder, resuspended in G-buffer (5 mM Tris-HCl [pH 7.5], 0.5 mM Dithiothreitol [DTT],
532 0.2 mM ATP, 0.1 mM $CaCl_2$), and then cleared by centrifugation for 20 min at 50,000 ×
533 g. The supernatant was filtered through Grade 1 Whatman paper, then the actin was
534 polymerized by the addition of 2 mM $MgCl_2$ and 50 mM NaCl and incubated overnight at
535 4°C. The final NaCl concentration was adjusted to 0.6 M to strip residual actin-binding
536 proteins, incubated at 4°C for 1 h, and then the F-actin was pelleted by centrifugation for
537 150 min at 361,000 × g. The pellet was solubilized by dounce homogenization and
538 dialyzed against 1 L of G-buffer at 4°C (three consecutive times at 12–18 h intervals).
539 Monomeric actin was then precleared at 435,000 × g and loaded onto a S200 (16/60)
540 gel-filtration column (GE Healthcare) equilibrated in G-Buffer. Peak fractions containing
541 actin were stored at 4°C.

542 To fluorescently label actin, G-actin was polymerized by dialyzing overnight
543 against modified F-buffer (20 mM PIPES [pH 6.9], 0.2 mM $CaCl_2$, 0.2mM ATP, 100 mM
544 KCl) (Shekhar, 2017). F-actin was incubated for 2 h at room temperature with Alexa 488
545 NHS ester dye (Life Technologies) at a final molar concentration 5 times in excess of
546 actin concentration. F-actin was then pelleted by centrifugation at 450,000 × g for 40
547 min at 4°C. The pellet was homogenized with a dounce and dialyzed overnight at 4°C

548 against 1 L of G-buffer (three consecutive times at 12–18 h intervals). Next, the solution
549 was centrifuged at 450,000 × g for 40 min at 4°C. The supernatant was collected and
550 loaded onto a S200 (16/60) gel-filtration column (GE Healthcare) equilibrated in G-
551 Buffer. Peak fractions containing labeled G-actin were pooled and the concentration and
552 labeling efficiency was determined by measuring the absorbance at 290 nm and 494
553 nm. Molar extinction coefficients used were as follows: ε_{290} actin = 26,600 M^{-1} cm^{-1} and
554 ε_{494} Alexa 488 = 71,000 M^{-1} cm^{-1}. The labeled G-actin was stored in G-Buffer + 50%
555 glycerol at -20°C and then dialyzed back into G-Buffer (no glycerol) for experiments.

556 **High-Speed and Low-Speed Pelleting (Co-Sedimentation) Assays**

557 F-actin was prepared by polymerizing 20 μM of G-actin with initiation mix (final
558 concentration: 2 mM $MgCl_2$, 0.5 mM ATP, 50 mM KCl) overnight at room temperature.
559 For high-speed pelleting assays, different concentrations of F-actin (0, 0.1, 0.25, 0.5, 1,
560 2, 4 μM) were incubated with 0.5 μM BtszB-CT for 30 min at room temperature.
561 Reactions were then centrifuged at 316,000 × g for 20 min at 25°C using a tabletop
562 Optima TLX Ultracentrifuge (Beckman Coulter). Supernatant and pellet fractions were
563 analyzed on Coomassie stained gels, and quantified by scanning densitometry using a
564 ChemiDoc Imaging System (BioRad). In calculating the fraction of BtszB-CT bound to
565 F-actin in each reaction, the BtszB-CT that pelleted nonspecifically (without F-actin) was
566 subtracted. Fraction of BtszB-CT bound at different concentrations of F-actin was
567 plotted, and fit to a Hill Equation using Prism (GraphPad). For low-speed pelleting
568 assays, 2 μM of F-actin was incubated with or without 1 μM BtszB-CT for 30 min at
569 room temperature. Reactions were then centrifuged at 16,000 × g for 10 min at room
570 temperature using a tabletop centrifuge (Eppendorf). Supernatant and pellet fractions

571 were analyzed on Coomassie stained gels and quantified as above. Fraction of F-actin
572 pelleted +/- BtszB-CT was plotted and compared statistically using a Mann-Whitney U
573 test from Prism (GraphPad).

574 **F-Actin Bundling TIRF Microscopy Assays and Image Analysis**

575 Glass coverslips (60 × 24 mm; Thermo Fisher Scientific) were first cleaned by
576 sonication in 1% Hellmanex™ III (Sigma-Aldrich) glass cleaner for 60 min at room
577 temperature, followed by successive sonications in 100% ethanol for 60 min and 1 M
578 KOH for 20 min. Coverslips were then washed extensively with H_2O and dried in an N_2
579 stream. The cleaned coverslips were coated with 2 mg/ml methoxy-polyethylene glycol
580 (PEG)-silane MW 2000 and 2 µg/ml biotin-PEG-silane MW 3400 (Laysan Bio, Arab, AL)
581 in 80% ethanol, pH 2.0, and incubated overnight at 70°C. Flow cells were assembled by
582 rinsing PEG-coated coverslips with water, drying with N_2, and adhering to µ-Slide VI0.1
583 (0.1 × 17 × 1 mm) flow chambers (Ibidi, Fitchburg, WI) with double-sided tape (2.5 cm ×
584 2 mm × 120 µm) and 5-min epoxy resin (Devcon, Danvers, MA). Before each reaction,
585 the flow cell was incubated for 1 min with 1% bovine serum albumin (BSA) in HEKG5
586 buffer (20 mM HEPES, pH 7.4, 1 mM EDTA, 50 mM KCl, and 5% glycerol), and then
587 equilibrated with TIRF buffer (10 mM imidazole, pH 7.4, 50 mM KCl, 1 mM $MgCl_2$, 1 mM
588 ethylene glycol-bis(β-aminoethyl ether)-N,N,N′,N′-tetraacetic acid (EGTA), 0.2 mM ATP,
589 10 mM DTT, 15 mM glucose, 20 µg/ml catalase, 100 µg/ml glucose oxidase) plus 0.5%
590 methylcellulose (4000 cP). Finally, 2 µM G-actin (10% Alexa 488–labeled on Cys 374)
591 polymerized to 10 - 20 µm, washed with TIRF buffer and then 1 µM BtszB-CT was
592 flowed into the reaction chamber 300 s after initiation of actin assembly. Upon flowing
593 wash TIRF buffer and BtszB-CT into the TIRF chamber, filament often would move

594 around but did not get flushed out because of the crowding agent (methylcellulose) in
595 the buffer.

596 Single-wavelength time-lapse TIRF imaging was performed on a Nikon-Ti2000
597 inverted microscope equipped with a 150-mW argon laser (Melles Griot), a 60 × TIRF
598 objective with a numerical aperture of 1.49 (Nikon Instruments), and an electron-
599 multiplying charge coupled device (EMCCD) camera (Andor Ixon, Belfast, Ireland). One
600 pixel was equivalent to 143 × 143 nm. Focus was maintained by the Perfect Focus
601 system (Nikon Instruments). TIRF microscopy images were acquired every 5 s and
602 exposed for 100 ms for at least 10 min using imaging software Elements (Nikon
603 Instruments, New York, NY).

604 Images were analyzed in FIJI version 2.0.0-rc-68/1.52e (National Institutes of
605 Health, Bethesda, MD). Background subtraction was conducted using the rolling ball
606 background subtraction algorithm (ball radius, 5 pixels). To measure actin filament
607 bundling, the line segment tool was used to draw a line perpendicular to actin
608 filaments/bundles in the FOV. The intensity profile of the line segment was fit to a 2-
609 dimensional Gaussian curve in FIJI. The intensity at full-width half-max (FWHM) for
610 each line trace was recorded at 300 s into the reactions (where BtszB-CT was flowed in
611 at time 0). All individual intensity measurements were normalized to the average actin
612 filament/bundle intensity from the control reaction (2 μM F-actin). A Mann-Whitney U
613 statistical test was performed to determine bundling activity between the control reaction
614 (2 μM F-actin) and the 1 μM BtsB-CT reaction.

615 **Statistical analysis**

616 All statistical analyses were carried out using GraphPad Prism or MATLAB.

Acknowledgments

We thank members of the Martin lab for helpful discussions and comments on the manuscript. We thank Jonathan Jackson for writing the segmentation pipeline code. We thank J. Solitro, Z. Li, and J. Eskin for their assistance with experiments. We are grateful to Goode lab members for assistance with actin purification and labeling. Finally, we thank the Bloomington Stock Center and the TRiP at Harvard Medical School (National Institutes of Health/National Institute of General Medical Sciences R01-GM084947) for providing fly stocks used in this study. This research was supported by a grant from the National Institutes of Health to B.L. Goode (R35 GM134895). This work is also supported by National Institutes of Health grants R01 GM105984 and R35 GM144115 to A.C. Martin.

References

Afshar, K., Stuart, B., Wasserman, S.A., 2000. Functional analysis of the *Drosophila* diaphanous FH protein in early embryonic development. Development 127, 1887–1897. https://doi.org/10.1242/dev.127.9.1887

Algrain, M., Turunen, O., Vaheri, A., Louvard, D., Arpin, M., 1993. Ezrin contains cytoskeleton and membrane binding domains accounting for its proposed role as a membrane-cytoskeletal linker. J. Cell Biol. 120, 129–139. https://doi.org/10.1083/jcb.120.1.129

Bajusz, C., Kristó, I., Abonyi, C., Venit, T., Vedelek, V., Lukácsovich, T., Farkas, A., Borkúti, P., Kovács, Z., Bajusz, I., Marton, A., Vizler, C., Lipinszki, Z., Sinka, R., Percipalle, P., Vilmos, P., 2021. The nuclear activity of the actin-binding Moesin protein is necessary for gene expression in Drosophila. FEBS J. 288, 4812–4832. https://doi.org/10.1111/febs.15779

Blankenship, J.T., Wieschaus, E., 2001. Two new roles for the Drosophila AP patterning system in early morphogenesis. Dev. Camb. Engl. 128, 5129–5138. https://doi.org/10.1242/dev.128.24.5129

Callaini, G., Dallai, R., Riparbelli, M.G., 1992. Cytochalasin induces spindle fusion in the syncytial blastoderm of the early *Drosophila* embryo. Biol. Cell 74, 249–254. https://doi.org/10.1016/0248-4900(92)90035-y

Camuglia, J.M., Yeh, A.R.A., Martin, A.C., 2021. Extracellular | Tension and Tissue Morphogenesis, in: Jez, J. (Ed.), Encyclopedia of Biological Chemistry III (Third Edition). Elsevier, Oxford, pp. 317–325.

Cant, K., Knowles, B.A., Mooseker, M.S., Cooley, L., 1994. *Drosophila* singed, a fascin homolog, is required for actin bundle formation during oogenesis and bristle extension. J. Cell Biol. 125, 369–380. https://doi.org/10.1083/jcb.125.2.369

Cao, J., Albertson, R., Riggs, B., Field, C.M., Sullivan, W., 2008. Nuf, a Rab11 effector, maintains cytokinetic furrow integrity by promoting local actin polymerization. J. Cell Biol. 182, 301–313. https://doi.org/10.1083/jcb.200712036

Carreno, S., Kouranti, I., Glusman, E.S., Fuller, M.T., Echard, A., Payre, F., 2008. Moesin and its activating kinase Slik are required for cortical stability and microtubule organization in mitotic cells. J. Cell Biol. 180, 739–746. https://doi.org/10.1083/jcb.200709161

Chou, T.B., Perrimon, N., 1992. Use of a yeast site-specific recombinase to produce female germline chimeras in *Drosophila*. Genetics 131, 643–653. https://doi.org/10.1093/genetics/131.3.643

Chugh, P., Paluch, E.K., 2018. The actin cortex at a glance. J. Cell Sci. 131, jcs186254. https://doi.org/10.1242/jcs.186254

Davidson, A.J., Millard, T.H., Evans, I.R., Wood, W., 2019. Ena orchestrates remodelling within the actin cytoskeleton to drive robust *Drosophila* macrophage chemotaxis. J. Cell Sci. 132, jcs224618. https://doi.org/10.1242/jcs.224618

Deneke, VE, Puliafito, A, Krueger, D, Narla, AV, De Simone, A, Primo, L, Vergassola, M, De Renzis, S, and Di Talia, S., 2019. Self-Organized Nuclear Positioning Synchronizes the Cell Cycle in Drosophila Embryos. Cell 177, 925-941.e17.

Foe, V.E., Field, C.M., Odell, G.M., 2000. Microtubules and mitotic cycle phase modulate spatiotemporal distributions of F-actin and myosin II in *Drosophila* syncytial blastoderm embryos. Development 127, 1767–1787. https://doi.org/10.1242/dev.127.9.1767

Frangi, A.F., Niessen, W.J., Vincken, K.L., Viergever, M.A., 1998. Multiscale vessel enhancement filtering. Springer Berlin Heidelberg, pp. 130–137.

Fukuda, M., 2002. The C2A domain of synaptotagmin-like protein 3 (Slp3) is an atypical calcium-dependent phospholipid-binding machine: comparison with the C2A domain of synaptotagmin I. Biochem. J. 366, 681–687. https://doi.org/10.1042/BJ20020484

Fukuda, M., Kuroda, T.S., Mikoshiba, K., 2002. Slac2-a/Melanophilin, the Missing Link Between Rab27 and Myosin Va: Implications of a Tripartite Protein Complex for Melanosome Transport. J. Biol. Chem. 277, 12432–12436. https://doi.org/10.1074/jbc.C200005200

Gálvez-Santisteban, M., Rodriguez-Fraticelli, A.E., Bryant, D.M., Vergarajauregui, S., Yasuda, T., Bañón-Rodríguez, I., Bernascone, I., Datta, A., Spivak, N., Young, K., Slim, C.L., Brakeman, P.R., Fukuda, M., Mostov, K.E., Martín-Belmonte, F., 2012. Synaptotagmin-like proteins control the formation of a single apical membrane domain in epithelial cells. Nat. Cell Biol. 14, 838–849. https://doi.org/10.1038/ncb2541

692 Gary, R., Bretscher, A., 1995. Ezrin self-association involves binding of an N-terminal
693 domain to a normally masked C-terminal domain that includes the F-actin binding
694 site. Mol. Biol. Cell 6, 1061–1075. https://doi.org/10.1091/mbc.6.8.1061
695 Goode, BL, Eskin, J, and Shekhar, S., 2023. Mechanisms of actin disassembly and
696 turnover. J Cell Biol 222, e202309021.
697 Gorfinkiel, N., Arias, A.M., 2007. Requirements for adherens junction components in the
698 interaction between epithelial tissues during dorsal closure in *Drosophila*. J. Cell
699 Sci. 120, 3289–3298. https://doi.org/10.1242/jcs.010850
700 Gould, K.L., Bretscher, A., Esch, F.S., Hunter, T., 1989. cDNA cloning and sequencing
701 of the protein-tyrosine kinase substrate, ezrin, reveals homology to band 4.1.
702 EMBO J. 8, 4133–4142. https://doi.org/10.1002/j.1460-2075.1989.tb08598.x
703 Gratz, S.J., Rubinstein, C.D., Harrison, M.M., Wildonger, J., O'Connor-Giles, K.M.,
704 2015. CRISPR-Cas9 Genome Editing in *Drosophila*. Curr. Protoc. Mol. Biol. 111,
705 31.2.1-31.2.20. https://doi.org/10.1002/0471142727.mb3102s111
706 Grevengoed, E.E., Fox, D.T., Gates, J., Peifer, M., 2003. Balancing different types of
707 actin polymerization at distinct sites: roles for Abelson kinase and Enabled. J.
708 Cell Biol. 163, 1267–1279. https://doi.org/10.1083/jcb.200307026
709 He, B., Martin, A., Wieschaus, E., 2016. Flow-dependent myosin recruitment during
710 *Drosophila* cellularization requires zygotic dunk activity. Development 143, 2417–
711 2430. https://doi.org/10.1242/dev.131334
712 Holly, R.M., Mavor, L.M., Zuo, Z., Blankenship, J.T., 2015. A rapid, membrane-
713 dependent pathway directs furrow formation through RalA in the early *Drosophila*
714 embryo. Development 142, 2316–2328. https://doi.org/10.1242/dev.120998
715 JayaNandanan, N., Mathew, R., Leptin, M., 2014. Guidance of subcellular
716 tubulogenesis by actin under the control of a synaptotagmin-like protein and
717 Moesin. Nat. Commun. 5, 3036. https://doi.org/10.1038/ncomms4036
718 Jiang, T., Harris, T.J.C., 2019. Par-1 controls the composition and growth of cortical
719 actin caps during *Drosophila* embryo cleavage. J. Cell Biol. 218, 4195–4214.
720 https://doi.org/10.1083/jcb.201903152
721 Jodoin, J.N., 2015. Stable Force Balance between Epithelial Cells Arises from F-Actin
722 Turnover. Dev. Cell 35, 685–697. https://doi.org/10.1016/j.devcel.2015.11.018
723 Koenderink, G.H., Paluch, E.K., 2018. Architecture shapes contractility in actomyosin
724 networks. Curr. Opin. Cell Biol. 50, 79–85.
725 https://doi.org/10.1016/j.ceb.2018.01.015
726 Krueger, D., Quinkler, T., Mortensen, S.A., Sachse, C., De Renzis, S., 2019. Cross-
727 linker–mediated regulation of actin network organization controls tissue
728 morphogenesis. J. Cell Biol. 218, 2743–2761.
729 https://doi.org/10.1083/jcb.201811127
730 Kuroda, T.S., Ariga, H., Fukuda, M., 2003. The Actin-Binding Domain of Slac2-
731 a/Melanophilin Is Required for Melanosome Distribution in Melanocytes. Mol.
732 Cell. Biol. 23, 5245–5255. https://doi.org/10.1128/MCB.23.15.5245-5255.2003
733 Lecuit, T., Samanta, R., Wieschaus, E., 2002. slam Encodes a Developmental
734 Regulator of Polarized Membrane Growth during Cleavage of the *Drosophila*
735 Embryo. Dev. Cell 2, 425–436. https://doi.org/10.1016/s1534-5807(02)00141-7
736 Lecuit, T., Yap, A.S., 2015. E-cadherin junctions as active mechanical integrators in
737 tissue dynamics. Nat. Cell Biol. 17, 533–539. https://doi.org/10.1038/ncb3136

Lyakhova, T.A., Knight, J.D., 2014. The C2 domains of granuphilin are high-affinity sensors for plasma membrane lipids. Chem. Phys. Lipids 182, 29–37. https://doi.org/10.1016/j.chemphyslip.2013.10.009

Maître, J.-L., Berthoumieux, H., Krens, S.F.G., Salbreux, G., Jülicher, F., Paluch, E., Heisenberg, C.-P., 2012. Adhesion Functions in Cell Sorting by Mechanically Coupling the Cortices of Adhering Cells. Science 338, 253–256. https://doi.org/10.1126/science.1225399

Martin, A.C., Gelbart, M., Fernandez-Gonzalez, R., Kaschube, M., Wieschaus, E.F., 2010. Integration of contractile forces during tissue invagination. J. Cell Biol. 188, 735–749. https://doi.org/10.1083/jcb.200910099

McCartney, B.M., McEwen, D.G., Grevengoed, E., Maddox, P., Bejsovec, A., Peifer, M., 2001. *Drosophila* APC2 and Armadillo participate in tethering mitotic spindles to cortical actin. Nat. Cell Biol. 3, 933–938. https://doi.org/10.1038/ncb1001-933

Mizuno, K., Fujita, T., Gomi, H., Izumi, T., 2016. Granuphilin exclusively mediates functional granule docking to the plasma membrane. Sci. Rep. 6, 23909. https://doi.org/10.1038/srep23909

Pilot, F., Philippe, J.-M., Lemmers, C., Chauvin, J.-P., Lecuit, T., 2006a. Developmental control of nuclear morphogenesis and anchoring by *charleston*, identified in a functional genomic screen of *Drosophila* cellularisation. Development 133, 711–723. https://doi.org/10.1242/dev.02251

Pilot, F., Philippe, J.-M., Lemmers, C., Lecuit, T., 2006b. Spatial control of actin organization at adherens junctions by a synaptotagmin-like protein Btsz. Nature 442, 580–584. https://doi.org/10.1038/nature04935

Plastino, J., Blanchoin, L., 2019. Dynamic stability of the actin ecosystem. J. Cell Sci. 132, jcs219832. https://doi.org/10.1242/jcs.219832

Postner, M.A., Wieschaus, E.F., 1994. The nullo protein is a component of the actin-myosin network that mediates cellularization in *Drosophila* melanogaster embryos. J. Cell Sci. 107, 1863–1873. https://doi.org/10.1242/jcs.107.7.1863

Riggs, B., Rothwell, W., Mische, S., Hickson, G.R.X., Matheson, J., Hays, T.S., Gould, G.W., Sullivan, W., 2003. Actin cytoskeleton remodeling during early *Drosophila* furrow formation requires recycling endosomal components Nuclear-fallout and Rab11. J. Cell Biol. 163, 143–154. https://doi.org/10.1083/jcb.200305115

Rikhy, R., Mavrakis, M., Lippincott-Schwartz, J., 2015. Dynamin regulates metaphase furrow formation and plasma membrane compartmentalization in the syncytial *Drosophila* embryo. Biol. Open 4, 301–311. https://doi.org/10.1242/bio.20149936

Roh-Johnson, M., Shemer, G., Higgins, C.D., McClellan, J.H., Werts, A.D., Tulu, U.S., Gao, L., Betzig, E., Kiehart, D.P., Goldstein, B., 2012. Triggering a Cell Shape Change by Exploiting Preexisting Actomyosin Contractions. Science 335, 1232–1235. https://doi.org/10.1126/science.1217869

Rothwell, W.F., Fogarty, P., Field, C.M., Sullivan, W., 1998. Nuclear-fallout, a *Drosophila* protein that cycles from the cytoplasm to the centrosomes, regulates cortical microfilament organization. Development 125, 1295–1303. https://doi.org/10.1242/dev.125.7.1295

Schejter, E.D., Wieschaus, E., 1993. bottleneck acts as a regulator of the microfilament network governing cellularization of the *Drosophila* embryo. Cell 75, 373–385. https://doi.org/10.1016/0092-8674(93)80078-S

Serano, J., Rubin, G.M., 2003. The *Drosophila* synaptotagmin-like protein bitesize is required for growth and has mRNA localization sequences within its open reading frame. Proc. Natl. Acad. Sci. 100, 13368–13373. https://doi.org/10.1073/pnas.1835727100

Shekhar, S., 2017. Microfluidics-Assisted TIRF Imaging to Study Single Actin Filament Dynamics. Curr. Protoc. Cell Biol. 77. https://doi.org/10.1002/cpcb.31

Sherlekar, A., Mundhe, G., Richa, P., Dey, B., Sharma, S., Rikhy, R., 2020. F-BAR domain protein Syndapin regulates actomyosin dynamics during apical cap remodeling in syncytial *Drosophila* embryos. J Cell Sci 133. https://doi.org/10.1242/jcs.235846

Simpson, L., Wieschaus, E., 1990. Zygotic activity of the nullo locus is required to stabilize the actin-myosin network during cellularization in *Drosophila*. Development 110, 851–863. https://doi.org/10.1242/dev.110.3.851

Sokac, A.M., Biel, N., De Renzis, S., 2023. Membrane-actin interactions in morphogenesis: Lessons learned from *Drosophila* cellularization. Semin. Cell Dev. Biol. 133, 107–122. https://doi.org/10.1016/j.semcdb.2022.03.028

Sokac, A.M., Wieschaus, E., 2008. Local Actin-Dependent Endocytosis Is Zygotically Controlled to Initiate *Drosophila* Cellularization. Dev. Cell 14, 775–786. https://doi.org/10.1016/j.devcel.2008.02.014

Spracklen, A.J., Fagan, T.N., Lovander, K.E., Tootle, T.L., 2014. The pros and cons of common actin labeling tools for visualizing actin dynamics during *Drosophila* oogenesis. Dev. Biol. 393, 209–226. https://doi.org/10.1016/j.ydbio.2014.06.022

Spracklen, A.J., Thornton-Kolbe, E.M., Bonner, A.N., Florea, A., Compton, P.J., Fernandez-Gonzalez, R., Peifer, M., 2019. The Crk adapter protein is essential for *Drosophila* embryogenesis, where it regulates multiple actin-dependent morphogenic events. Mol. Biol. Cell 30, 2399–2421. https://doi.org/10.1091/mbc.e19-05-0302

Spudich, J.A., Watt, S., 1971. The Regulation of Rabbit Skeletal Muscle Contraction: I. BIOCHEMICAL STUDIES OF THE INTERACTION OF THE TROPOMYOSIN-TROPONIN COMPLEX WITH ACTIN AND THE PROTEOLYTIC FRAGMENTS OF MYOSIN. J. Biol. Chem. 246, 4866–4871. https://doi.org/10.1016/S0021-9258(18)62016-2

Stevenson, V., Hudson, A., Cooley, L., Theurkauf, W.E., 2002. Arp2/3-Dependent Psuedocleavage Furrow Assembly in Syncytial *Drosophila* Embryos. Curr. Biol. 12, 705–711. https://doi.org/10.1016/S0960-9822(02)00807-2

Stevenson, V.A., Kramer, J., Kuhn, J., Theurkauf, W.E., 2001. Centrosomes and the Scrambled protein coordinate microtubule-independent actin reorganization. Nat. Cell Biol. 3, 68–75. https://doi.org/10.1038/35050579

Sullivan, W., Fogarty, P., Theurkauf, W., 1993. Mutations affecting the cytoskeletal organization of syncytial *Drosophila* embryos. Development 118, 1245–1254. https://doi.org/10.1242/dev.118.4.1245

Tam, R., Harris, T.J.C., 2024. Centrosome-organized plasma membrane infoldings linked to growth of a cortical actin domain. J. Cell Biol. 223, e202403115. https://doi.org/10.1083/jcb.202403115

Tilney, L.G., Connelly, P.S., Vranich, K.A., Shaw, M.K., Guild, G.M., 2000. Regulation of Actin Filament Cross-Linking and Bundle Shape in *Drosophila* Bristles. J. Cell Biol. 148, 87–99.

Vilmos, P., Jankovics, F., Szathmári, M., Lukácsovich, T., Henn, L., Erdélyi, M., 2009. Live imaging reveals that the Drosophila actin-binding ERM protein, moesin, co-localizes with the mitotic spindle. Eur. J. Cell Biol. 88, 609–619. https://doi.org/10.1016/j.ejcb.2009.05.006

Vilmos, P., Kristó, I., Szikora, S., Jankovics, F., Lukácsovich, T., Kari, B., Erdélyi, M., 2016. The actin-binding ERM protein Moesin directly regulates spindle assembly and function during mitosis. Cell Biol. Int. 40, 696–707. https://doi.org/10.1002/cbin.10607

Webb, R.L., Zhou, M.-N., McCartney, B.M., 2009. A novel role for an APC2-Diaphanous complex in regulating actin organization in *Drosophila*. Development 136, 1283–1293. https://doi.org/10.1242/dev.026963

Wenzl, C., Yan, S., Laupsien, P., Großhans, J., 2010. Localization of RhoGEF2 during *Drosophila* cellularization is developmentally controlled by slam. Mech. Dev. 127, 371–384. https://doi.org/10.1016/j.mod.2010.01.001

Xie, Y., Budhathoki, R., Blankenship, J.T., 2021. Combinatorial deployment of F-actin regulators to build complex 3D actin structures in vivo. eLife 10. https://doi.org/10.7554/elife.63046

Zallen, J.A., Cohen, Y., Hudson, A.M., Cooley, L., Wieschaus, E., Schejter, E.D., 2002. SCAR is a primary regulator of Arp2/3-dependent morphological events in *Drosophila*. J. Cell Biol. 156, 689–701. https://doi.org/10.1083/jcb.200109057

Zaman, R., Lombardo, A., Sauvanet, C., Viswanatha, R., Awad, V., Bonomo, L.E.-R., McDermitt, D., Bretscher, A., 2021. Effector-mediated ERM activation locally inhibits RhoA activity to shape the apical cell domain. J. Cell Biol. 220, e202007146. https://doi.org/10.1083/jcb.202007146

Zhang, Y., Yu, J.C., Jiang, T., Fernandez-Gonzalez, R., Harris, T.J.C., 2018. Collision of Expanding Actin Caps with Actomyosin Borders for Cortical Bending and Mitotic Rounding in a Syncytium. Dev. Cell 45, 551-564.e4. https://doi.org/10.1016/j.devcel.2018.04.024

Zheng, L., Sepúlveda, L.A., Lua, R.C., Lichtarge, O., Golding, I., Sokac, A.M., 2013. The Maternal-to-Zygotic Transition Targets Actin to Promote Robustness during Morphogenesis. PLoS Genet. 9, e1003901. https://doi.org/10.1371/journal.pgen.1003901

866 ## Figures and Figure Legends

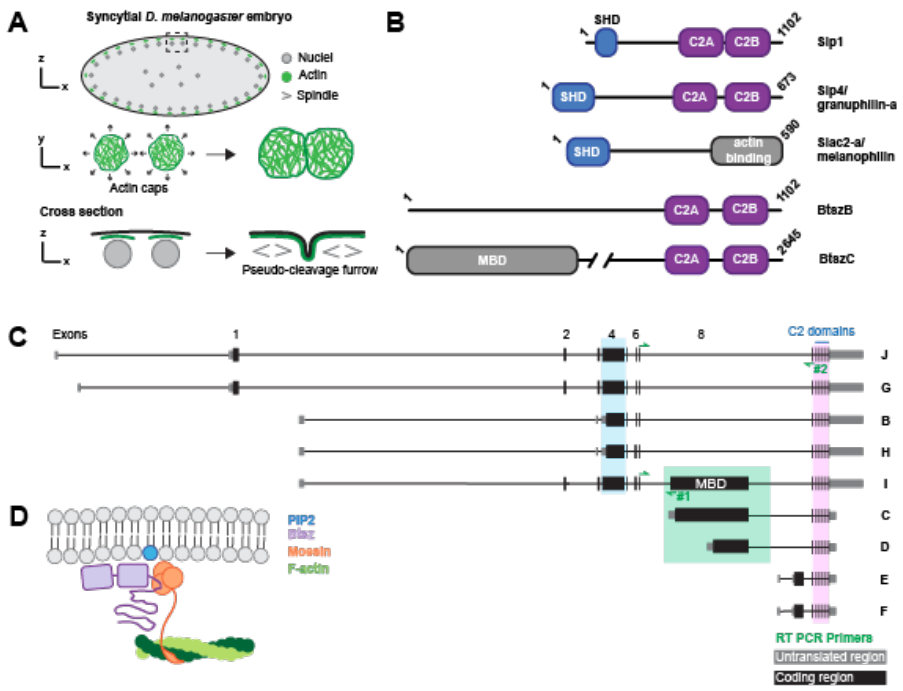

867
868 Figure 1. **Btsz is a Synaptotagmin-like protein (Slp) with multiple splice isoforms. (A)**
869 Cartoon depiction of a syncytial embryo during a nuclear cycle. Sagittal plane through a
870 syncytial embryo (top row). Zoomed in view of the actin caps in the dashed rectangular box
871 where actin caps grow and collide with neighboring actin caps (middle row). Cross section of the
872 zoomed in view where pseudo-cleavage furrows form from actin caps that have collided (bottom
873 row). **(B)** Schematic of mammalian (mouse) Slp1, Slp4, Slac2-a, and fly Btsz isoform B and C
874 proteins. **(C)** Schematic of the nine splice isoforms of the Btsz protein. Letters on the left-hand
875 side denote the isoform name. Location of isoform-specific RT-PCR primer pairs #1 and #2 for
876 non-MBD (BtszJ, G, B, and H) and BtszI, respectively, are shown with green arrows. **(D)** Model
877 depicting Btsz's interaction with the plasma membrane and Moesin. Btsz and Moesin localized
878 to apical membrane through interactions with PIP2. There, Btsz can bind the FERM domain of
879 Moesin and Moesin binds F-actin.

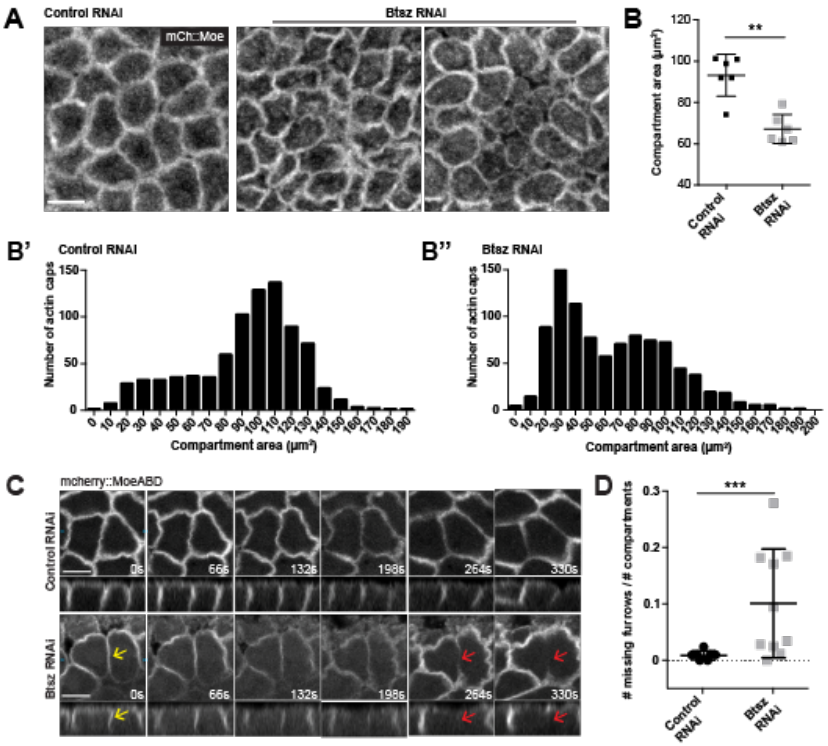

Figure 2. **Btsz is required for actin remodeling during syncytial blastoderm development. (A)** Maximum projection of a top-down view of control and Btsz RNAi nuclear cycle 12 actin caps. Actin was visualized live using the mCherry::MoesinABD marker. **(B)** In Btsz-depleted embryos, the average cap size is smaller compared to those in the control. Each data point is an average of all caps in the field of view per embryo. n = 6 embryos for both control RNAi and Btsz RNAi. p = 0.0043, Mann-Whitney U test. **(B', B'')** Histogram of raw data of actin cap area from Figure 2B. There is a peak of small actin caps (~30 μm^2) in Btsz RNAi embryos that is absent in the control embryos. **(C)** Time-lapse showing the formation of pseudo-cleavage furrows in control and Btsz-depleted embryos during nuclear cycle 12, with single slices (top panels) and orthogonal views (bottom panels). Actin was visualized live using the mCherry::MoesinABD marker. In Btsz RNAi embryo, a pseudo-cleavage furrow forms normally (yellow arrows), but breaks and recedes (red arrows) during metaphase while neighboring furrows are at their maximum length. **(D)** Number of missing furrows normalized over total number of actin caps during nuclear cycle 12. In Btsz-depleted embryos, pseudo-cleavage

895 furrows prematurely recede during mitosis more often than in wild type embryos. Each point is
896 the ratio of missing furrows to actin caps in a field of view (212 x 106 μm) per embryo. n = 7
897 embryos for control RNAi, n = 10 embryos for Btsz RNAi, p = 0.0007, Mann-Whitney U test.
898 Scale bars are 10 μm.
899

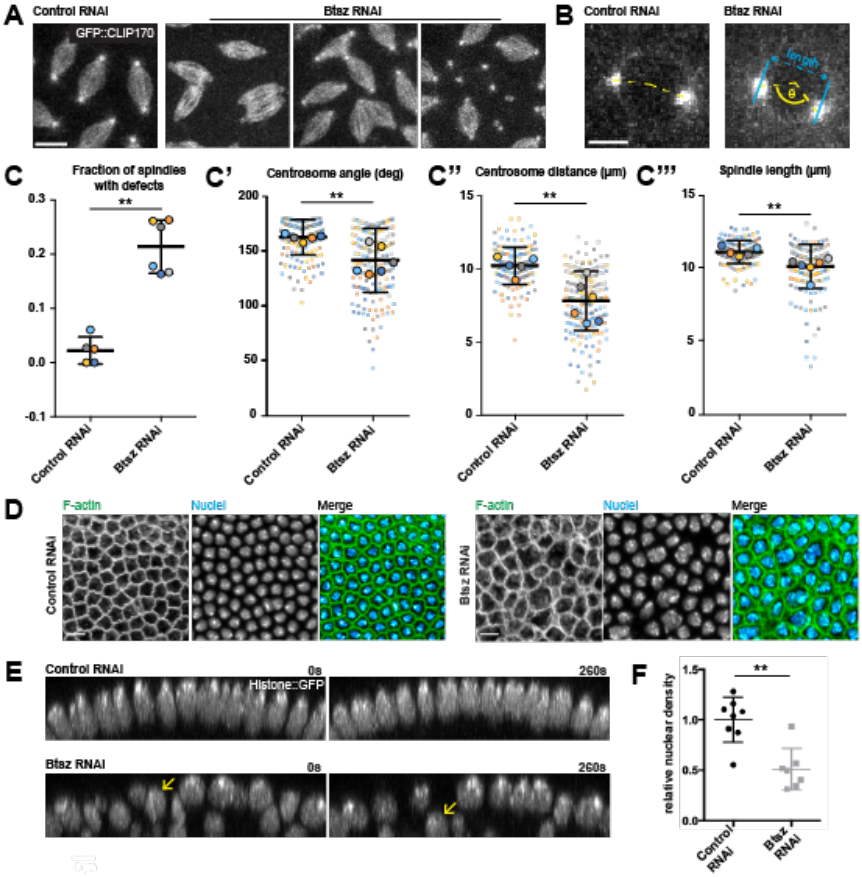

Figure 3. **Btsz-depletion leads to spindle collision and nuclear defects. (A, B)** Maximum projections of nuclear cycle 11 spindles and centrosomes visualized live using GFP::CLIP170 in control and Btsz-depleted embryos. Spindle collisions and aberrant centrosome morphology occur more frequently in Btsz RNAi embryos. Scale bars are 10 µm for spindles, 5 µm for centrosomes. **(C)** Fraction of spindles that have collided in control and Btsz RNAi embryos. Each large, bold circle is the fraction of occurrences in an embryo **(C'-C''')** Quantification of shortest distance between a centrosome pair (cyan line), angle of a vertex drawn between a centrosome pair (yellow dashed line), and spindle length. Each large, bold circle is the average of one embryo and smaller circles of corresponding color are the centrosome pairs or individual spindles used in the analysis. n = 5 embryos for control RNAi, n = 6 embryos for Btsz RNAi. p = 0.0043 for fraction with defects, 0.0087 for centrosome distance and angle, 0.0043 for spindle length, Mann-Whitney U test. **(D)** Single sagittal slice of control RNAi or Btsz RNAi embryos during early cellularization. F-actin was visualized using Phalloidin and nuclei was visualized

using Hoechst in fixed samples. Both the actin cytoskeleton and nuclei are abnormal in Btsz RNAi embryos. **(E)** Orthogonal slice of nuclei visualized live using Histone::GFP at cellularization in control (top) or Btsz RNAi (bottom) embryos at 0s and 260s later. Yellow arrow indicates one nucleus at the surface of the Btsz RNAi embryo undergoing fallout. **(F)** Nuclear fallout occurs more frequently in Btsz-depleted embryos compared to the control. Each point is the number of nuclei over area (nuclear density) in one embryo. $p = 0.0043$, Mann-Whitney U test.

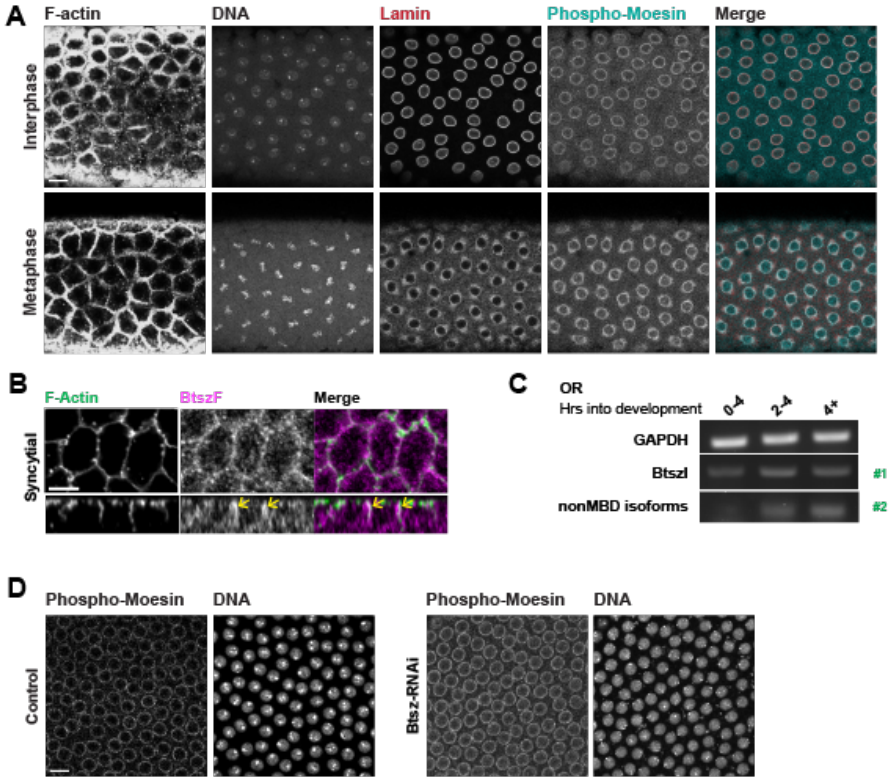

Figure 4. **Btsz has function(s) in the syncytium that do not depend on localizing Moesin**. **(A)** Optical section of the F-actin network, DNA, Lamin B, and phospho-Moesin localization in the wild-type syncytium at interphase and at metaphase. Phospho-Moesin localizes to perinuclear regions, closely overlapping with Lamin B. **(B)** Maximum projection of a top-down view of the F-actin network and Btsz isoform F localization in the syncytium. BtszF localizes to pseudo-cleavage furrows (yellow arrows). **(C)** Gel of RT-PCR products measuring isoform expression over developmental time. Both non-MBD isoforms and MBD isoforms are upregulated during the maternal to zygotic transition (MZT). Primer pair #1 detected Btszl and primer pair #2 detected non-MBD isoforms, as indicated in green. **(D)** Optical section of phospho-Moesin localization during interphase is similar for wild-type and Btsz-RNAi syncytium. Scale bars: A, D, 10 μM; B, 5 μm.

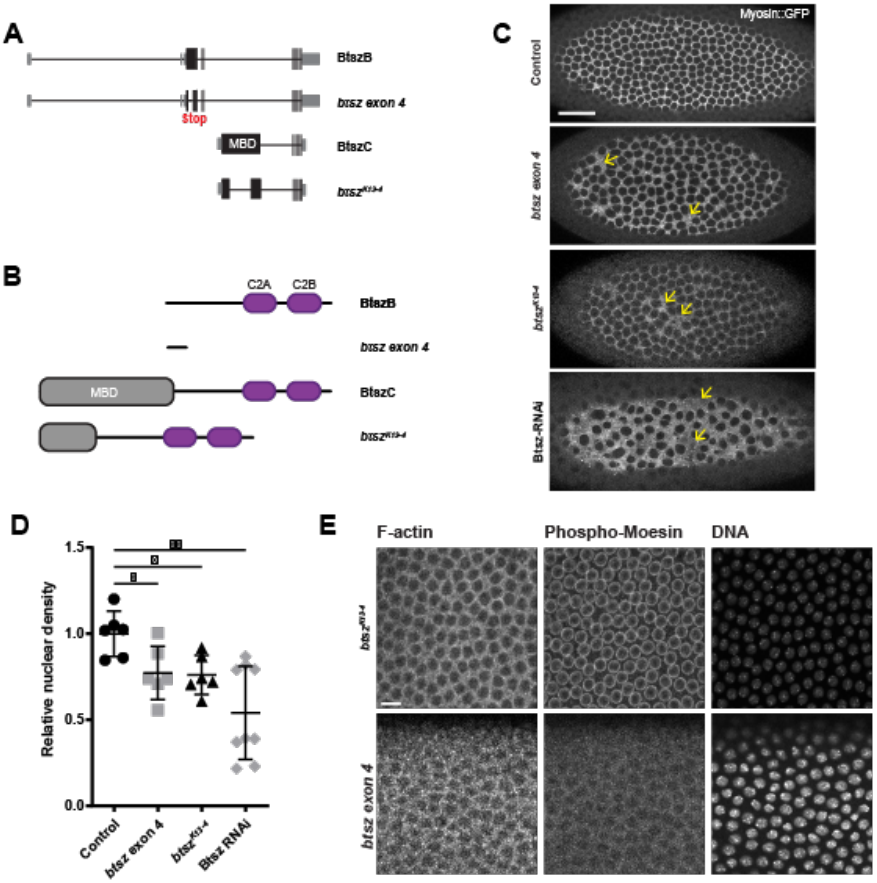

Figure 5. **Non-MBD and MBD containing Btsz isoforms are important for development**. **(A)** Schematic of Btsz isoforms B and C, along with Btsz mutants *btsz exon 4 (*which was generated in this study) and *btsz^{K13-4}*. *btsz exon 4* has an early truncation in exon 4, and *btsz^{K13-4}* has a deletion in exon 8. **(B)** Schematic of the protein products of the Btsz isoforms and mutants shown in (B). **(C)** Maximum projection images of cellularizing live embryos expressing Spaghetti squash::GFP (Sqh::GFP). Labeling myosin allows for visualization of the cytoskeletal network between nuclei enabling robust nuclear density determination. Yellow arrows indicate gaps where nuclei have dropped out that have been filled in by the myosin network. Scale bar is 25 µm. **(D)** Relative nuclear density in *btsz exon 4* and *btsz^{K13-4}* mutants, compared to controls. p = 0.0260 for both comparisons, Mann-Whitney U test. **(E)** Grazing slices of cortical nuclei in syncytial embryo. F-actin was visualized using Phalloidin, nuclei was visualized using Hoechst, and Phospho-Moesin with anti-pMoe in fixed samples. Scale bar is 10 µm.

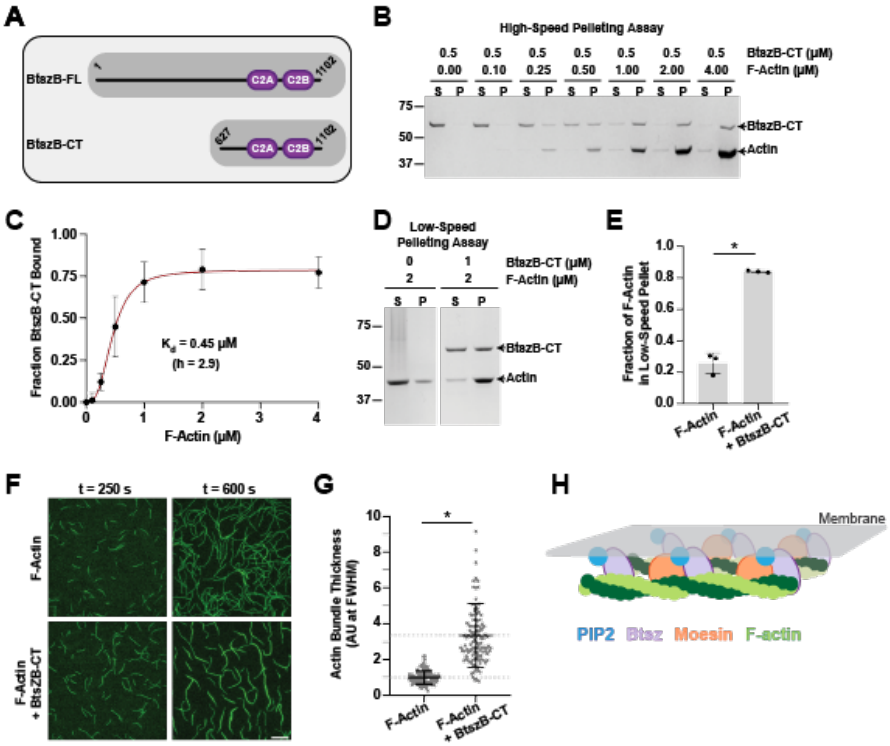

Figure 6. **The C-terminus of BtszB cooperatively binds and bundles actin filaments. (A)** Schematic of full length BtszB (BtszB-FL) for reference and the C-terminal fragment (BtszB-CT) that was used in the F-actin binding and bundling assays. **(B)** High-speed F-actin co-sedimentation assay varying the F-actin concentration (0.1 - 4 μM) in the presence of 0.5 μM BtszB-CT. F-actin and BtszB-CT samples were incubated together at room temperature for 30 min and then centrifuged (20 min at 25°C, 316k x g). **(C)** The fraction of BtszB-CT bound to actin filaments at increasing concentrations of F-actin was fit to a cooperative binding model with a K_d of 0.45 μM and a hill coefficient (h) of 2.9. Error bars are SD, n = 3. **(D)** Low-speed F-actin co-sedimentation assay using 2 μM F-actin with and without 1 μM BtszB-CT. F-actin and BtszB-CT were mixed together and incubated at room temperature for 30 min, then centrifuged (10 min at room temperature, 16k x g). **(E)** The fraction of F-actin pelleted with and without BtszB-CT. Error bars are SD, n = 3. p-value < 0.001, Student's t-test. **(F)** Representative time-lapse images from TIRF microscopy reactions containing 2 μM G-actin (10% Alexa 488-labeled) polymerized into filaments 10-20 μm in length, and then buffer or 1 μM BtszB-CT was flowed into the reaction chamber at 300 s and monitored for an additional 300 s. Scale bar is 20 μm. **(G)** Filament/bundle thickness was assessed by measuring the fluorescence intensity at FWHM (full width at half maximum) from line segments drawn perpendicular to the filament or bundle. Fluorescence intensity values were

normalized to the mean intensity value of the control reaction (2 μM F-actin). Horizontal dashed lines are at y = 1, mean 2 μM F-actin control reaction, and y = 3.4, mean 2 μM F-actin + 1 μM BtszB-CT. ($n_{experiments}$ = 3, $n_{line\ segment}$ measurements for 2 μM F-actin = 41, 40, 42 and 1 μM BtszB-CT = 24, 35, 57. Error bars are SD, * is p-value < 0.001, Mann-Whitney U test). **(H)** Schematic of how Btsz non-MBD and MBD isoforms may interact with Moesin and/or F-actin at the membrane to bundle and organize the cytoskeleton.

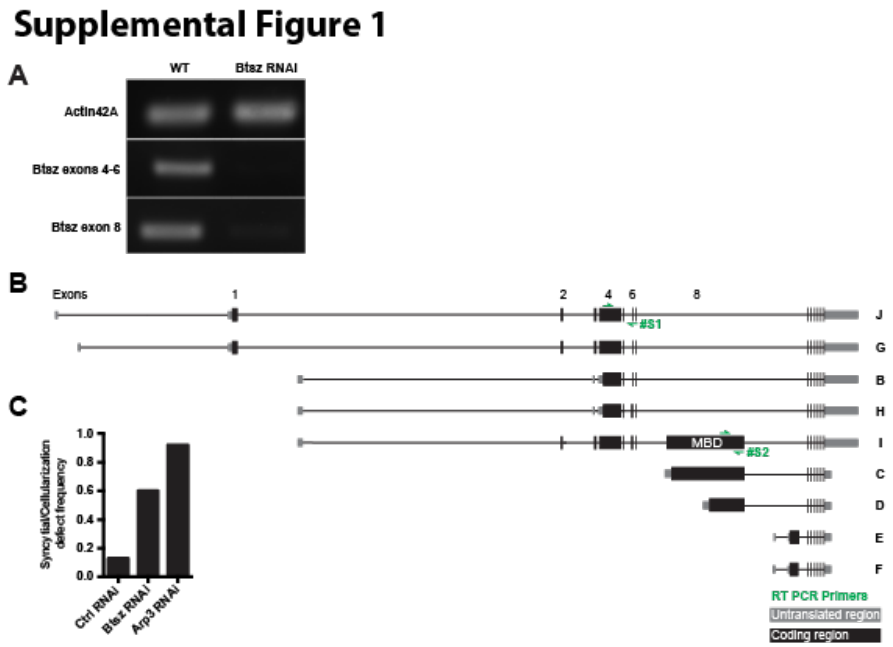

Supplemental Figure 1. (A) RT-PCR Gel of Btsz cDNA showing maternal knockdown of Btsz in the early embryo. Primers used are shown in S1B. Primer pair S1 was used for Btsz exons 4-6 and pair S2 was used for Btsz exon 8, the MBD. **(B)** Schematic of the nine splice isoforms of the Btsz protein. Letters on the right-hand side denote the isoform name. Location of RT-PCR primer pairs #S1 and #S2 for exons 4-6 and exon 8, respectively, are shown with green arrows. **(C)** Frequency of control RNAi, Btsz RNAi, and Arp3 RNAi embryos with defects during the syncytial or cellularization stages. 4 out

983 of 30 control, 25 out of 42 Btsz RNAi, and 12 out of 13 Arp3 RNAi embryos displayed
984 defects.
985

Supplemental Figure 2

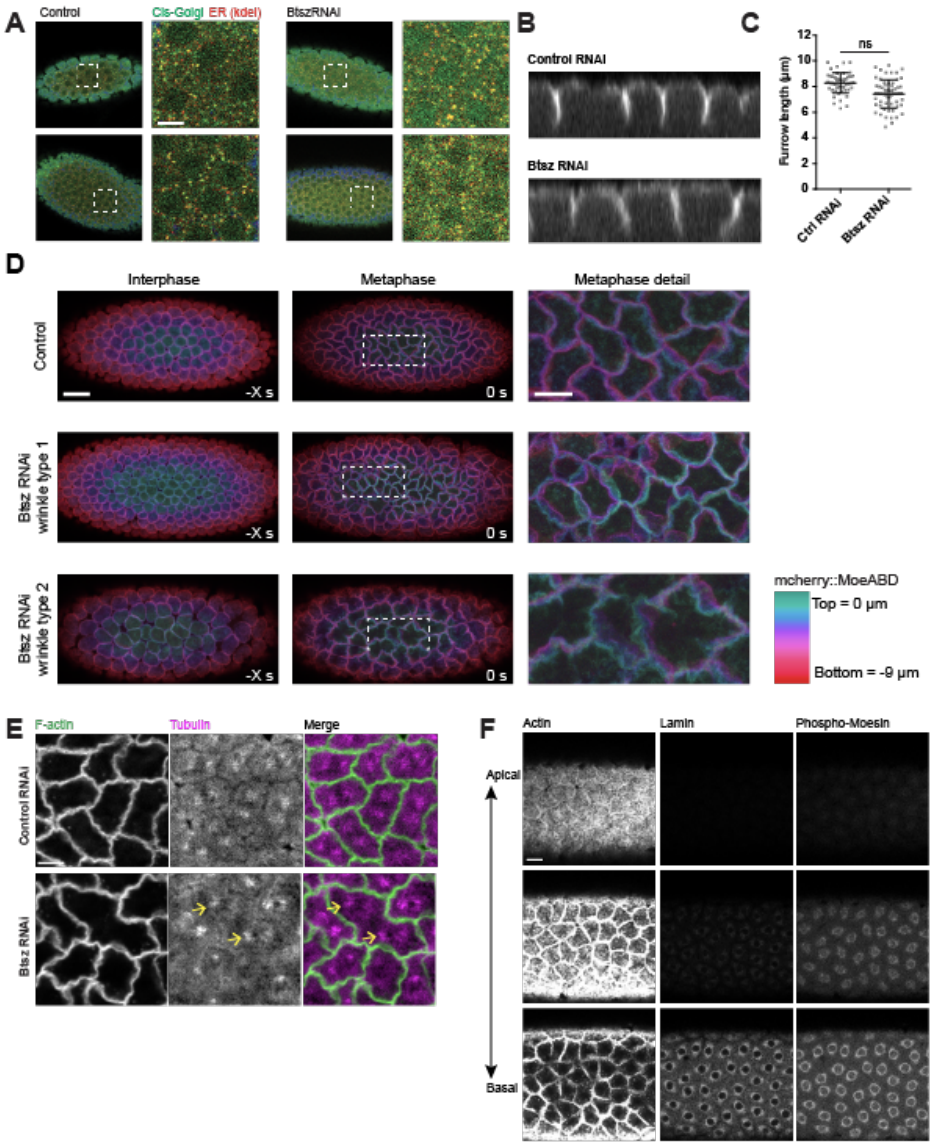

Supplemental Figure 2. (A) Maximum intensity projections of cortical grazing slices of control and Btsz-RNAi embryos stained for ER (anti-KDEL) and Cis-golgi (anti-gm130). Morphology and overlap between stained compartments were not disrupted in Btsz-RNAi. Scale bar = 5 µm. **(B)** Cross section of pseudo-cleavage furrows during syncytial blastoderm development. Actin was visualized live with the mCherry::MoesinABD marker. **(C)** Pseudo-cleavage furrows that form normally in Btsz RNAi embryos are not significantly different in length compared to the wildtype. Each point is one furrow from n = 6 embryos for both control RNAi and Btsz RNAi. **(D)** Intensity projection of mCherry::MoesinABD with different depths encoded by color (right, colormap). Control embryos have tight distribution of colors, while Btsz-RNAi embryos often have

1000 dispersed color signals indicating tilted or wavy pseudo-cleavage furrow morphology.
1001 **(E)** Slice of fixed wildtype and Btsz RNAi embryos during metaphase. F-actin was
1002 visualized using Phalloidin and tubulin was visualized using an α-tubulin antibody.
1003 Pseudo-cleavage furrows that have receded lead to two sets of spindles in one
1004 compartment (yellow arrows). Scale bar is 5 µm. **(F)** Grazing sections of the F-actin
1005 network (Phalloidin), Lamin B, and phospho-Moesin in the wild-type syncytium at metaphase at
1006 dfferent depths. Phospho-Moesin localizes to perinuclear regions, closely overlapping with
1007 Lamin B and is absent from F-actin caps and pseudo-cleavage furrows.
1008

Supplemental Figure 3

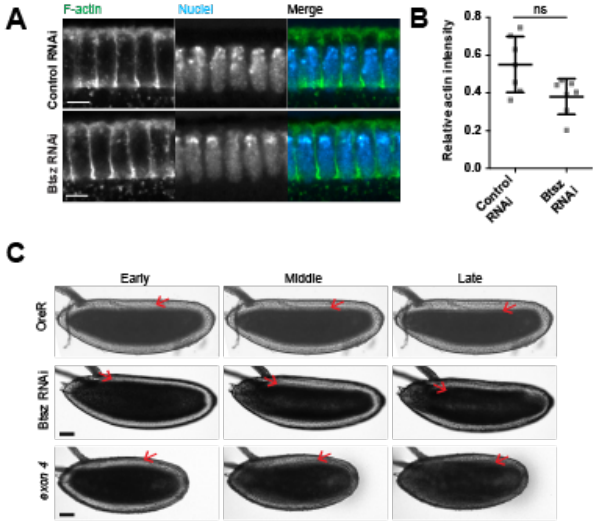

Supplemental Figure 3 (A) Cross section of fixed control RNAi or Btsz-RNAi embryos during cellularization. F-actin was visualized using Phalloidin and nuclei were visualized using Hoechst. Scale bar = 5μm. **(B)** There is no significant difference between the relative F-actin intensity (ratio of actin intensity in the apical region to that of the furrow canals) in the wildtype and Btsz-RNAi embryos. Mann-Whitney U test. **(C)** Brightfield images of control, btsz-RNAi, and btsz[exon4] mutant embryos undergoing cellularization. Red arrows indicate cellularization front. Note that cellularization front is often uneven in Btsz-RNAi and btsz mutant embryos, likely due to nuclear fallout and density defects.

Supplemental Figure 4

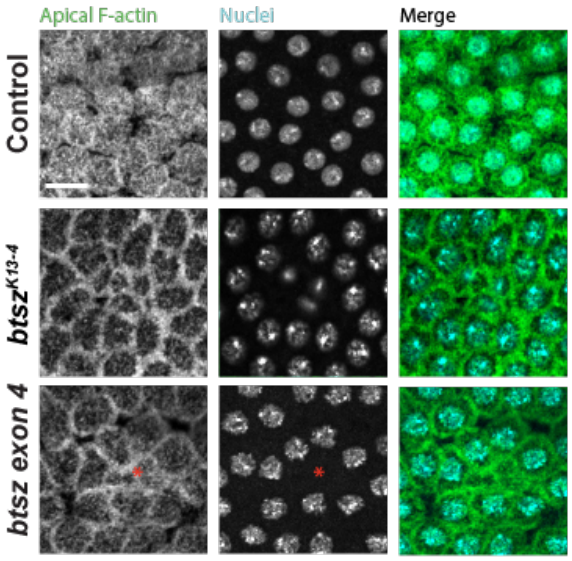

Supplemental Figure 4. Btsz mutants have syncytial embryos defects. Images are grazing sections showing cortical F-actin (phalloidin staining) and nuclei (Hoechst staining) in control and btsz[k13-4] and btsz[exon4] mutants. Note that mutants exhibit regions that lack nuclei under actin caps (red asterisk), similar to the nuclear fallout phenotype of Btsz-RNAi. Scale bar = 10 μm.